Journal of Materials Chemistry A

Highly Active and Stable Nickel-Molybdenum Nitride (Ni2Mo3N) Electrocatalyst for Hydrogen Evolution

Journal:	*Journal of Materials Chemistry A*
Manuscript ID	TA-ART-10-2020-010090.R1
Article Type:	Paper
Date Submitted by the Author:	22-Jan-2021
Complete List of Authors:	Park, Sang Heon; Kangwon National University, Chemical Engineering Jo, Tae Hwan; Kangwon National University, Chemical Engineering Lee, Min Hee; Ulsan National Institute of Science and Technology Kawashima, Kenta; University of Texas at Austin, Department of Chemistry Mullins, Charles; University of Texas at Austin, Department of Chemical Engineering Lim, Hyung-Kyu; Kangwon National University, Division of Chemical Engineering and Bioengineering Youn, Duck Hyun; Kangwon National University, Chemical Engineering

ARTICLE

Highly Active and Stable Nickel-Molybdenum Nitride (Ni_2Mo_3N) Electrocatalyst for Hydrogen Evolution

Received 00th January 20xx,
Accepted 00th January 20xx

DOI: 10.1039/x0xx00000x

Sang Heon Park,[#a] Tae Hwan Jo,[#a] Min Hee Lee,[b] Kenta Kawashima,[c] C. Buddie Mullins,[*c] Hyung-Kyu Lim,[*a] and Duck Hyun Youn[*a]

This paper reports a highly active and stable nonprecious metal electrocatalyst based on bimetallic nanoscale nickel molybdenum nitride developed for the hydrogen evolution reaction (HER). A composite of 7 nm Ni_2Mo_3N nanoparticles grown on nickel foam (Ni_2Mo_3N/NF) was prepared through a simple and economical synthetic method involving one-step annealing of Ni foam, $MoCl_5$, and urea without a Ni precursor. The Ni_2Mo_3N/NF exhibits high activity with low overpotential (η_{10} of 21.3 mV and η_{100} of 123.8 mV) and excellent stability for the HER, achieving one of the best performances among state-of-the-art transition metal nitride based catalysts in alkaline media. Supporting density functional theory (DFT) calculations indicate that N sites in Ni_2Mo_3N with a N-Mo coordination number of four have a hydrogen adsorption energy close to that of Pt and hence may be responsible for the enhanced HER performance.

Introduction

Hydrogen is a promising alternative to fossil fuels due to its high energy density, abundance, and sustainability. Among diverse hydrogen production routes, electrochemical water splitting combined with renewable energy sources (solar or wind power) is attracting much attention due to low cost, simplicity, and zero emission of greenhouse gases and pollutants.[1–4] For further development of the electrochemical water splitting system, efficient electrocatalysts are required for both the anodic oxygen evolution reaction (OER) and the cathodic hydrogen evolution reaction (HER). Platinum based materials are the best catalysts, particularly for the HER, but high cost and scarcity limit large scale applications.[5–7] Thus, developing non-noble metal based electrocatalysts for the HER to substitute for Pt based materials is essential.

Transition metal nitrides (TMNs) have unique physical properties, including hardness, wear resistance, and superconductivity, as well as for use as coating agents for cutting tools and refractory materials.[8,9] They also have shown enhanced catalytic activities in various heterogeneous reactions (hydrodesulfurization and hydrogenation) and energy applications (fuel cells, photocatalytic systems, and solar cells) due to the similarity of their electronic structures to noble metals.[10-15] TMNs such as Mo_2N and CoN have been recently considered as potential HER catalysts,[16,17] and further HER activity enhancement has been achieved by employing bimetallic TMNs. The presence of a second metal atom in bimetallic TMNs could provide more reaction sites and improve electronic conductivity compared to monometallic TMNs.[18,19] Nickel molybdenum nitrides (Ni-Mo-N) are representative bimetallic TMNs with high HER activity. Ni atoms are recognized as efficient water dissociation sites, and Mo atoms have a strong binding energy towards hydrogen. Thus, the synergy between Ni and Mo in Ni-Mo-N can effectively reduce the energy barrier of the Volmer step and enhance HER activity under alkaline media.[19-21]

Herein, we report an efficient HER electrocatalyst in alkaline media comprising bimetallic Ni_2Mo_3N and Ni foam. *Via* the simple annealing of a Mo precursor, Ni foam, and urea in one-pot, nanostructured Ni_2Mo_3N was directly grown on the Ni foam (Ni_2Mo_3N/NF), and the catalyst exhibits remarkably high activity and stability for the HER. The Ni_2Mo_3N/NF catalyst offers several advantages in terms of its synthesis and HER performance: 1) The Ni_2Mo_3N catalyst has been rarely reported previously,[1,22,23] with most bimetallic Ni-Mo-N studies investigating $Ni_{0.2}Mo_{0.8}N$ catalysts.[19,24-29] Thus, the synthetic method and study of Ni_2Mo_3N/NF as a HER catalyst presented here are unique. 2) The proposed synthetic method is much simpler and more economical than reported methods. Previous bimetallic Ni-Mo-N catalysts have typically required multiple steps in their preparation, bimetallic oxide fabrication using Mo and Ni precursors, and Ni foams by hydrothermal treatment followed by annealing with NH_3 gas.[22,24,26,28-32] In contrast, the proposed synthesis involved reacting a Mo precursor ($MoCl_5$) with urea followed by annealing with Ni foams in one-pot under a N_2 atmosphere to obtain the Ni_2Mo_3N/NF electrocatalyst. A Ni

[a] Department of Chemical Engineering, Interdisciplinary Program in Advanced Functional Materials and Devices Development, Kangwon National University, Chuncheon, Gangwon-do 24341, South Korea. Email:youndh@kangwon.ac.kr (D.H. Youn), hklim@kangwon.ac.kr (H.-K. Lim)
[b] School of Energy and Chemical Engineering, Ulsan National Institute of Science and Technology (UNIST), Ulsan 44919, South Korea.
[c] McKetta Department of Chemical Engineering and Department of Chemistry, Center for Electrochemistry, University of Texas at Austin, 1 University Station, C0400 Austin, TX 78712-0231, United States. Email:mullins@che.utexas.edu
# These authors contributed equally to this study.
† Electronic Supplementary Information (ESI) available: [XRD, SEM-EDS, TEM, XPS, N_2-sorption, LSV, CV, CA and simulation results]. See DOI: 10.1039/x0xx00000x

precursor is not necessary because Ni atoms are released from the Ni foam during annealing, and toxic NH_3 gas is not required.[5,33,34] Thus, the proposed synthesis method is simple, economical and environmentally friendly. 3) The prepared Ni_2Mo_3N/NF catalyst achieves one of the best performances among the TMN-based catalysts for the HER, with low overpotentials (21.3 mV @10 mA cm^{-2} and 123.8 mV @ 100 mA cm^{-2}) and great durability for 24 h. Furthermore, the Ni_2Mo_3N/NF electrocatalyst displayed HER activity nearly as good as platinum, with even higher activity at potential over 100 mV in alkaline solution. In addition, we report on the origin of the HER activity employing first-principles density functional theory (DFT), in which nitrogen sites in Ni_2Mo_3N with coordination number 4 are shown to have a favorable H-adsorption energy (that is close to Pt) and this factor is likely responsible for the enhanced HER performance. Herein we describe a simple strategy for the synthesis of a bimetallic TMN on a Ni foam substrate which is a highly efficient HER electrocatalyst.

Experimental

Synthesis of Ni_2Mo_3N/NF.

3.66 mmol $MoCl_5$ (Aldrich) was dissolved in 2.53 mL ethanol, then 5.49 mmol urea (molar ratio urea/Mo = 1.5) was added to the solution under stirring for 1 h until the urea was completely dissolved. The solution was transferred to an alumina boat with pieces of Ni foam (Goodfellow) and annealed at 600 ℃ (ramping at 3.3 ℃ min^{-1}) for 3 h under flowing N_2 gas (100 sccm) to fabricate the Ni_2Mo_3N/NF electrocatalyst. For comparison, Mo_2N catalyst was synthesized by an identical method except Ni foam was omitted during synthesis. The fabricated Mo_2N catalyst was drop casted onto Ni foam to make the Mo_2N/NF electrocatalyst. The loading amount of Ni_2Mo_3N and Mo_2N on NF was ca. 10 mg cm^{-2}.

Characterization.

Crystalline structures of the prepared catalysts were investigated by X-ray diffraction (XRD, PANalytical X'pert PRO). Scanning electron microscope (SEM, Hitachi, S-4800) with an energy dispersive X-ray spectrometer (EDS) and high resolution transmission electron microscope (HRTEM, JEOL JEM-2100F) were used to reveal detailed structural information. Surface chemical states were analyzed using X-ray photoelectron spectroscopy [XPS, Thermo Fisher Scientific, K-Alpha (X-ray source: Al-$K_{\alpha1}$)]. The recorded binding energies were calibrated using the C 1s peak of advantageous carbon at 284.4 eV. Catalyst surface area and pore size distribution were characterized by N_2 adsorption-desorption isotherms measured at 77 K (Micromeritics, ASAP 2020 Plus).

Electrochemical Tests.

Electrochemical characterizations were carried out in a three-electrode cell system with N_2-saturated aqueous 1 M KOH solution using a potentiostat (PAR, VersaSTAT 4). The electrocatalyst loaded Ni foam (1×1 cm^2) was directly used as a working electrode. The Ag/AgCl (3 M NaCl) and Pt wire were used as reference and counter electrodes, respectively. All potentials were converted to the reversible hydrogen electrode (RHE) using the equation ($E_{RHE} = E_{Ag/AgCl} + 0.059\ pH + E^o_{Ag/AgCl}$). Linear sweep voltammetry (LSV) polarization curves were obtained with iR compensation at a scan rate of 5 mV s^{-1}. Electrochemical impedance spectroscopy (EIS) was performed over 10^5 to 10^{-1} Hz with a modulation amplitude of 5 mV at 50 mV overpotential, and EIS plots were fitted by Z-view software.

Computational Simulation.

Density functional theory calculations were performed using Quantum ESPRESSO software,[35] the generalized gradient approximation of Perdew-Burke-Ernzerhof (GGA-PBE) was used as the exchange-correlation functional.[36] The electron-ion interactions were handled using the projector-augmented-wave (PAW) potentials, and plane-wave energy was used up to 40 Ry. The surface model was created by applying 15 Å vacuum in a normal direction to the surface. A dipole correction scheme was applied to minimize the electronic interaction between periodic images. The Monkhorst-Pack grid (2×2×1) was used for the reciprocal space sampling. Vibrational frequency calculations were made for H_2 molecules and H-adsorption structures to calculate H-adsorption free energy. Average correction (+0.31 eV) was added to H-adsorption energy derived from the self-consistent field energy.

Results and discussion

Fig. 1 shows a schematic illustration for the fabrication of a Ni_2Mo_3N/NF catalyst. Ni foam was employed as a support for Ni_2Mo_3N nanoparticles since it has a high electrical conductivity and porous hierarchical structure, providing a conductive pathway for electron flow and allowing facile electrolyte interaction with catalytically active sites.[37,38] Molybdenum chloride ($MoCl_5$) dissolved in ethanol and urea (molar ratio urea/Mo = 1.5) as a nitrogen source were added together to form a viscous Mo-urea complex. Ni foam and the Mo-urea complex were placed in an alumina boat together and annealed at 600 ℃ for 3 h under N_2 flow to obtain the Ni_2Mo_3N nanoparticles supported on nickel foam (i.e., Ni_2Mo_3N/NF).Conventional Ni-Mo-N composite fabrication methods involved multiple steps (hydrothermal followed by annealing with NH_3 gas), whereas the proposed method grew nanostructured Ni_2Mo_3N directly on Ni foam *via* a simple one-pot synthesis. A Ni precursor was not required, since Ni foam acted as the Ni source, releasing Ni atoms during annealing.[39-42] Notably, the resultant Ni_2Mo_3N is a rarely reported crystalline phase for study as an electrocatalyst for the HER. The Ni_2Mo_3N

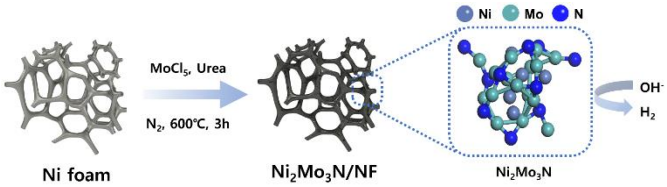

Fig. 1. Schematic illustration of the synthetic metod for Ni_2Mo_3N/NF

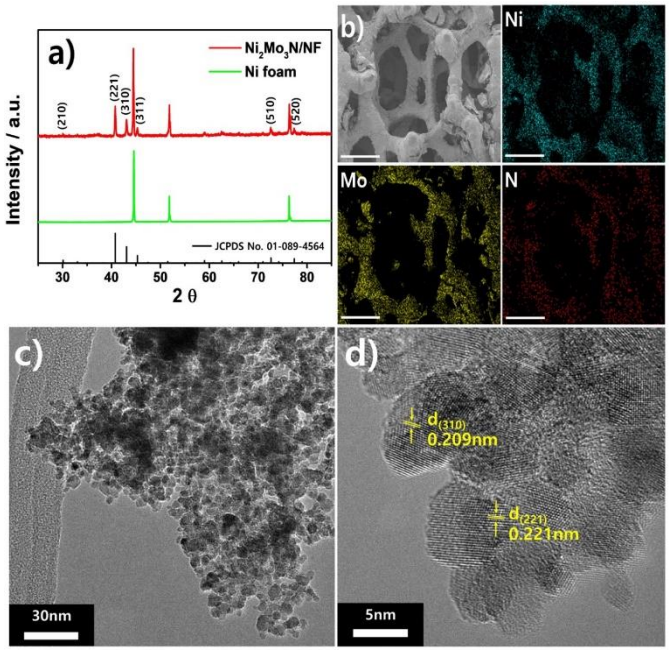

Fig. 2. Ni_2Mo_3N/NF characterization results: a) XRD patterns; b) SEM-EDS elemental mapping images (scale bar = 300 µm); c) and d) TEM images.

particles adopt a filled β-manganese structure comprising corner-sharing Mo_6N octahedra and interpenetrated net-like Ni atoms.[43,44] Thus, the simple synthetic route is straightforward and economical reducing reaction time and experimental effort substantially.

Fig. 2a shows the X-ray diffraction (XRD) patterns for Ni_2Mo_3N/NF. The intense peaks at 45, 52, and 75° originate from cubic Ni (JCPDS No. 00-004-0850) and the other peaks were assigned to the cubic Ni_2Mo_3N (JCPDS No. 01-089-4564) phase. No impurity peaks were observed, such as metal oxides or monometallic nitrides, indicating that phase-pure Ni_2Mo_3N was successfully grown on the Ni foam.

Fig. 2b shows the scanning electron microscope (SEM) and corresponding energy dispersive X-ray spectrometry (EDS) elemental mapping images. The three-dimensional porous structure of the Ni foam is clearly observed as a rough surface due to the Ni_2Mo_3N growth on the Ni foam. The elemental mapping images of Ni, Mo, and N were generally consistent with each other, indicating the uniform Ni_2Mo_3N formation on the Ni foam. Incidentally, the pristine Ni foam did not exhibit Mo and N signals (Fig. S1). To further examine the morphological and crystallographic details, transmission electron microscope (TEM) analysis was performed on the Ni_2Mo_3N/NF. Fig. 2c shows that the Ni_2Mo_3N on the Ni foam consists of small nanoparticles with a mean particle size of 7 nm, and Fig. 2d shows interplanar distances of 0.221 and 0.209 nm, corresponding to cubic Ni_2Mo_3N (221) and (310) planes, respectively. In another TEM image in Fig. S2, all observed lattice distances are well matched with Ni_2Mo_3N phase, further confirming the formation of Ni_2Mo_3N.

Fig. 3 shows the X-ray photoelectron spectroscopy (XPS) spectra of the Ni_2Mo_3N/NF catalyst. The survey spectrum confirms Ni, Mo, N, and O elemental presence, where O

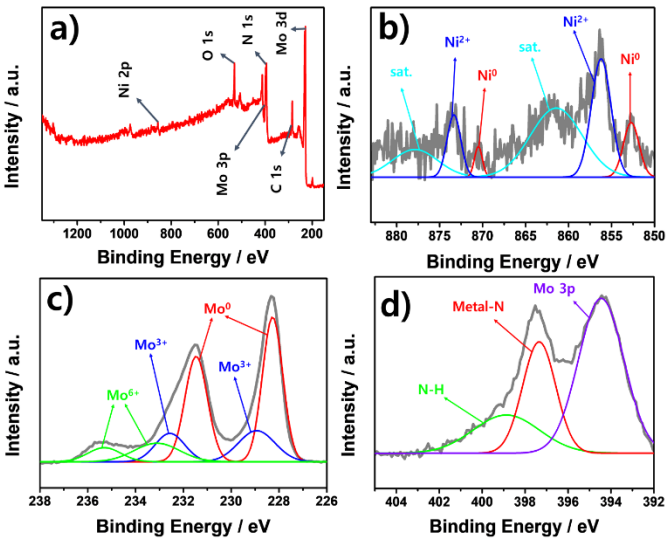

Fig. 3. XPS spectra of Ni_2Mo_3N/NF for a) survey, b) Ni 2p, c) Mo 3d, and d) N 1s.

elements can be attributed to surface oxidation upon air exposure (Fig. 3a). Two intense peaks in the Ni 2p spectra at 856.2 and 873.3 eV with a satellite peak at 861.4 and 877.9 eV were assigned to Ni^{2+} $2p_{3/2}$ and Ni^{2+} $2p_{1/2}$, respectively (Fig. 3b), and the weak peaks at 852.7 and 870.5 eV were assigned to metallic Ni.[23,45] Fig. 3c shows three Mo oxidation states: Mo^0 (228.3 and 231.5 eV), Mo^{3+} (228.9 and 232.6 eV) and Mo^{6+} (233.1 and 235.3 eV).[22,23,25-27,46] The Mo^{3+} species correspond to metal nitride, whereas the presence of Mo^{6+} species could be due to surface oxide formation.[26,47] In the N 1s spectrum (Fig. 3d), the deconvoluted peak at 397.3 eV originates from the lattice nitrogen species in a metal nitride and the peak at 398.9 eV corresponds to the N-H group. The Mo 3p and N 1s peaks partially overlap, hence Mo 3p peaks appear at 394.5 eV.[19,22,45]

Textural properties for Ni_2Mo_3N/NF were investigated by N_2 adsorption-desorption isotherms (Fig. S3). Ni_2Mo_3N/NF exhibits a Type IV isotherm indicating the presence of mesopores, whereas pristine Ni foam did not show clear adsorption-desorption characteristics. The Brunauer-Emmett-Teller (BET) surface area for Ni_2Mo_3N/NF and pristine Ni foam was 17.328 and 0.014 $m^2 g^{-1}$, respectively (Fig. S3a). Additionally, a pore size distribution (PSD) was determined using a desorption isotherm measured by the Barrett-Joyner-Halenda (BJH) method. The average pore size is about 13 nm in Ni_2Mo_3N/NF (Fig. S3b).

Fig. 4a shows the polarization curve for Ni_2Mo_3N/NF (1×1 cm^2) in 1 M KOH solution along with commercial 20 wt% Pt/C (BASF, lot#: F0381022, casted on rotating disk electrode) and pristine Ni foam curves for comparison. The Ni_2Mo_3N/NF exhibited remarkably high activity, comparable to the commercial Pt/C electrocatalyst. A η_{10} value (overpotential to drive 10 mA cm^{-2}) of 21.3 mV was recorded, close to that for Pt/C (η_{10} = 18.2 mV). Further, the η_{50} and η_{100} values of the Ni_2Mo_3N/NF are 89 and 123.8 mV, respectively. In particular, at an overpotential over ca. 100 mV, the Ni_2Mo_3N/NF showed higher current density than the Pt/C. In addition, Pt/C catalyst casted on Ni foam (Pt/C/NF, 10 mg cm^{-2} Pt/C on NF) recorded 17.1, 59.4, 91.7 mV for η_{10}, η_{50}, and η_{100} values, respectively (Fig. S4a). At the same

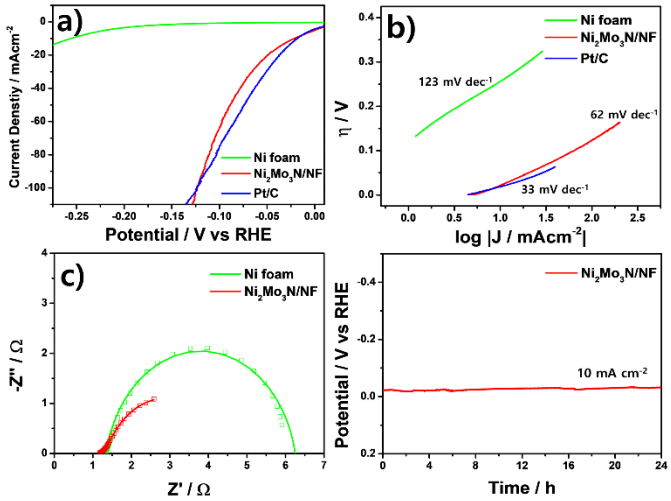

Fig. 4. Electrochemical characterization for the prepared catalysts. a) Polarization curves, b) Tafel plots, c) Nyquist plots, and d) stability measurement.

catalyst loading on NF, the Pt/C/NF showed higher activity than that of the Ni_2Mo_3N/NF. However, considering the high cost and low loading of Pt/C catalyst in current electrolyzers (< 1 mg cm^{-2}),[48-50] the Pt/C/NF is not practical.

The pristine Ni foam showed quite low HER activity over the entire potential region with an η_{10} value of 256.3 mV, confirming that the high HER activity is due to the Ni_2Mo_3N phase. This HER performance is amongst the best state-of-the-art TMN-based catalysts (Table S1). The high HER activity likely was a result of the synergy between the highly active Ni_2Mo_3N phase and the electrically conductive and porous Ni foam which provided a highly conductive pathway for electron flow and a large surface area for electrolyte access. Interestingly, monometallic Mo_2N nanoparticles supported on nickel foam (i.e., Mo_2N/NF) exhibit much lower activity (η_{10} = 109.7 mV, η_{50} = 190 mV, η_{100} = 223.7 mV) than the Ni_2Mo_3N/NF electrocatalyst (Fig. S4b) suggesting the importance of the bimetallic nature of the active sites on the catalyst.

Fig. 4b shows Tafel plots for the catalysts, where the Tafel slope was determined from the Tafel equation ($\eta = b\log|J| + a$, in which η is the overpotential, b is the Tafel slope, and J is the current density). The Tafel slope for Ni_2Mo_3N/NF is 62 mV dec^{-1}, which indicates that the electrochemical reaction follows the Volmer-Heyrovsky mechanism and proton desorption is the rate-determining step.[6,51] The Pt/C and Ni foam have Tafel slope values of 33 and 123 mV dec^{-1}, respectively.

The electrochemical active surface area (ECSA) was evaluated by the double-layer capacitance (C_{dl}) method (Fig. S5). The measured C_{dl} value for Ni_2Mo_3N/NF is 375.09 mF cm^{-2}, 100 times higher than that for the pristine Ni foam (3.26 mF cm^{-2}), which is generally consistent with the N_2-sorption results (Fig. S3). The high ECSA achieved after Ni_2Mo_3N growth on the Ni foam reflects the improved contact area between the catalyst and electrolyte, an important beneficial factor for enhancing the Ni_2Mo_3N/NF HER activity.

Electrochemical impedance spectroscopy (EIS) was conducted for further characterization of the prepared catalysts. The obtained Nyquist plots are displayed in Fig. 4c. A semicircle in the Nyquist plot originates from the charge-transfer resistance (R_{ct}) and corresponding capacitance, describing the charge-transfer process at the catalyst/electrolyte interface. In general, the R_{ct} value is inversely proportional to the electrocatalytic activity. The R_{ct} values of the Ni_2Mo_3N/NF and pristine Ni foam were 2.916 and 5.222 Ω, respectively, reflecting the high activity of the Ni_2Mo_3N/NF for the HER. And, the C_{dl} values estimated from EIS were 431.05 mF cm^{-2} for the Ni_2Mo_3N/NF, which is 2 order of magnitude higher compared to 2.96 mF cm^{-2} for the Ni foam. The trend is similar with the C_{dl} values obtained from CVs (Fig. S5).

Long-term stability is another important criterion for HER electrocatalysts, hence we conducted chronopotentiometric studies to investigate the durability of the prepared catalyst. The HER activity for Ni_2Mo_3N/NF was maintained at 10 mA cm^{-2} for 24 h without significant potential change (Fig. 4d). Moreover, the Ni_2Mo_3N/NF achieved stable performances for 10 h at even higher current densities (50 and 100 mA cm^{-2}, Fig. S6). These results lead us to conclude that the Ni_2Mo_3N/NF catalyst has excellent electrochemical durability for the HER.

Various analyses were conducted to investigate structural changes in the Ni_2Mo_3N/NF electrocatalyst after the 24 h durability test. Fig. S7 shows that the characteristic XRD peaks for the Ni_2Mo_3N phase remained after the durability test, indicating the structural stability of the Ni_2Mo_3N/NF. The SEM images in Fig. S8 confirm that the Ni_2Mo_3N/NF morphology after the durability test was generally consistent with that of the fresh Ni_2Mo_3N/NF electrocatalyst. In addition, EDS elemental mapping images continue to show the uniform distribution of Ni, Mo, and N after the durability test (Fig. S9). Fig. S10a shows the TEM images of the Ni_2Mo_3N/NF after the durability test. The Ni_2Mo_3N nanoparticles with an average particle size of 7 nm were observed without apparent aggregation. In a high resolution TEM (HRTEM) image (Fig. S10b), the lattice distances of 0.221 and 0.209 nm were detected, corresponding to the (221) and (310) planes of the Ni_2Mo_3N particles, respectively. Thus, there were no significant changes in structure and morphology of the Ni_2Mo_3N/NF catalyst after the durability tests, verifying its HER stability.

Fig. S11 displays the XPS spectra for Ni_2Mo_3N/NF after the durability test. In the Ni 2p spectra (Fig. S11b), the Ni^0 peak disappeared and Ni^{2+} peak intensities increased possibly due to the formation of NiO and $Ni(OH)_2$. Here, the three pairs of peaks were detected at 854.3/872, 856.6/874.1, and 861/877.8 eV corresponding to the Ni^{2+} $2p_{3/2}$/Ni^{2+} $2p_{1/2}$ doublets of NiO, $Ni(OH)_2$, and satellites, respectively.[27-29,45] Mo 3d XPS spectra (Fig. S11c) show Mo^0 (228.3/231.4 eV), Mo^{3+} (229/232.1 eV), Mo^{4+} (229.8/232.9 eV), Mo^{5+} (231.1/234.3 eV), and Mo^{6+} (233/236.1 eV) species with increased oxide species.[21-23,25-27,46,52] In the N 1s XPS spectra (Fig. S11d), the peaks attributed to metal nitride and N-H were maintained at 397.5 and 399 eV, respectively after the durability test.[19,22,45]

To investigate the origin of the HER activity for the Ni_2Mo_3N/NF electrocatalyst at the atomic level, DFT calculations were performed. Based on the (221) surface, the most dominant peak in the XRD pattern, several stoichiometric

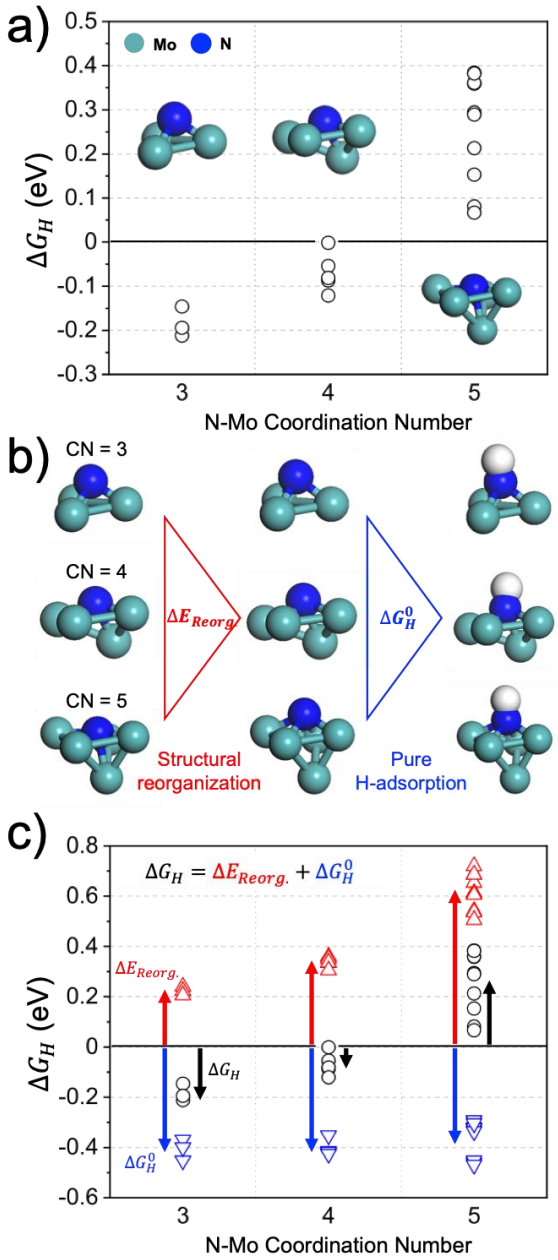

Fig. 5. DFT results for nitrogen active sites to explain enhanced HER activity: a) overall H-adsorption strength trend with respect to coordination number (CN) of N-Mo bonding, b) changes in local structure of active site during H-adsorption process, c) energy component analysis with respect to CN. Turquoise, blue, and white spheres represent Mo, N, and H atoms, respectively.

surfaces ($Ni_{24}Mo_{36}N_{12}$) were generated, ensuring the absence of dangling atoms or kinks. Hydrogen adsorption (H-adsorption) energies (ΔG_H) were calculated for possible Ni, Mo, and N active sites for three of the most stable surfaces, as shown in Fig. S12. Ni and Mo are open-metal sites and H-adsorption strengths were expected to be strong. The calculated ΔG_H for three arbitrary Ni and Mo sites on the most stable surface (Surf. 1) indicates that strong H-adsorption (ΔG_H = -0.47 to -0.15 eV) occur predominantly in the intermediate positions between Ni and Mo (Fig. S13). Thus, Ni and Mo are not the expected HER active sites due to their much stronger H-adsorption compared to thermal neutral conditions ($\Delta G_H = 0$ eV), which is the ideal H-adsorption strength for ideal HER activity.[53]

The active site was expected to be at the N atom rather than Ni or Mo,[26] considering the high HER activity of the Ni_2Mo_3N/NF electrocatalyst. Therefore, ΔG_H values were calculated for six different N sites for three surface models (a total of 18 N sites). The obtained H-adsorption energies for N sites are in a range from -0.21 to 0.38 eV, passing through the thermal neutral condition for an active site to show high HER performance. By analyzing the detailed local structure of the N active sites, a good correlation between N-Mo coordination number (CN) and ΔG_H was observed (Fig. 5a). The N atom exhibits three distinct CN's (3, 4, and 5) on these surfaces, and as the CN increases the N is more deeply embedded in the Mo network and stabilized, hence decreasing the H-adsorbed bond strength.

The local structure of N active sites exhibited significant structural change accompanied with the H-adsorption process. To analyze H-adsorption characteristics with respect to CN, the adsorption was separated into two processes: 1) structural reorganization of the active site, and 2) pure H-adsorption steps (Fig. 5b). The energy change for the former process ($\Delta E_{Reorg.}$) can be defined as energy difference between the frozen state (H is removed from the final structure) and the bare surface state (energy required for distortion of N-Mo local structure in the H-adsorption process). The energy change in the second process (ΔG_H^0) is the pure H-adsorption energy after reorganization of the active site. The overall H-adsorption energy can be expressed as the sum of energies, as follows:

$$\Delta G_H = \Delta E_{Reorg.} + \Delta G_H^0$$

Fig. 5c shows that ΔG_H^0 values were nearly constant regardless of CN (average -0.38 eV), consistent with its physical meaning; whereas $\Delta E_{Reorg.}$ values were dependent on CN, exhibiting a similar trend to ΔG_H. In the case of CN = 5, a substantial energy was required (average 0.62 eV) due to the large distortion of the N-Mo bonding network (bond cleavage between N and bottom Mo), compared with the cases of CN = 3 and 4 (average 0.22 and 0.34 eV, respectively), where changes in the local structure were less pronounced. Hence, the active sites with CN = 4 exhibited an appropriate balance between local structure reorganization and H-binding, resulting in a H-adsorption energy (average -0.07 eV) close to the thermally neutral condition. Therefore, N active sites with a specific CN (*i.e.*, 4) exhibited high HER performance, which was comparable to a Pt electrocatalyst (ΔG_H = -0.05 eV for Pt (111)).

Conclusions

We investigated a simple method for fabricating a Ni_2Mo_3N/NF nonprecious bimetallic electrocatalyst for the hydrogen evolution reaction. The synthetic process involves one-step annealing of a mixture of a Mo precursor and urea and Ni foam (with no need for a Ni precursor), which is straightforward and economical compared with more typical two-step annealing (e.g., hydrothermal and nitridation) methods. The resultant Ni_2Mo_3N/NF electrocatalyst, which is comprised of 7 nm

Ni_2Mo_3N nanoparticulates and Ni foam, achieved a remarkably high HER activity with low overpotentials (η_{10} = 21.3 mV and η_{100} = 123.8 mV) and excellent stability for 24 h, retaining one of the best performances amongst state-of-the-art TMN-based catalysts. Our DFT calculations suggested that structural characteristics of the N active sites affect the HER activity, and in particular, the N sites with a coordination number if 4 had the proper H-adsorption energy (i.e., close to that for Pt) for facile proton reduction. Considering the simple and economical fabrication route and the high electrochemical performance, the proposed Ni_2Mo_3N/NF could be a promising electrocatalyst for the HER step in a water-splitting process.

Conflicts of interest

There are no conflicts to declare.

Acknowledgements

This research was supported by the Basic Science Research Program through the National Research Foundation of Korea funded by the Ministry of Education (NRF) (grant 2019R1I1A3A01052741), the Technology Development Program to Solve Climate Changes through the NRF (grant 2018M1A2A2061994), the National Science Foundation of the United States (grant CHE-1664941) and the Robert A. Welch Foundation (grant F-1436). Material characterizations were conducted at the Central Laboratory of Kangwon National University.

Notes and references

1 W. F. Chen, K. Sasaki, C. Ma, A. I. Frenkel, N. Marinkovic, J. T. Muckerman, Y. Zhu and R. R. Adzic, *Angew. Chem., Int. Ed. Engl.,* 2012, **51**, 6131-6135.
2 C. G. Morales-Guio, L. A. Stern and X. Hu, *Chem. Soc. Rev.,* 2014, **43**, 6555-6569.
3 J. A. Turner, *Science*, 2004, **305**, 972-974.
4 S. A. Bonke, M. Wiechen, D. R. MacFarlane and L. Spiccia, *Energy Environ. Sci.*, 2015, **8**, 2791-2796.
5 G. H. Lee, M. H. Lee, Y. Kim, H.-K. Lim and D. H. Youn, *J. Alloys Compd.*, 2019, **805**, 113-119.
6 F. Safizadeh, E. Ghali and G. Houlachi, Int. J. Hydrogen Energy, 2015, **40**, 256-274.
7 J. Mohammed-Ibrahim and X. Sun, *J. Energy Chem.*, 2019, **34**, 111-160.
8 D. Ham and J. Lee, *Energies*, 2009, **2**, 873-899.
9 R. S. Ningthoujam and N. S. Gajbhiye, *Prog. Mater. Sci.*, 2015, **70**, 50-154.
10 J. Xie and Y. Xie, *Chem. Eur. J.*, 2016, **22**, 3588-3598.
11 W. F. Chen, J. T. Muckerman and E. Fujita, *Chem. Commun.*, 2013, **49**, 8896-8909.
12 X. Peng, C. Pi, X. Zhang, S. Li, K. Huo and P. K. Chu, *Sustain. Energy Fuels*, 2019, **3**, 366-381.
13 D. H. Youn, G. Bae, S. Han, J. Y. Kim, J.-W. Jang, H. Park, S. H. Choi and J. S. Lee, *J. Mater. Chem. A*, 2013, **1**, 8007-8015.
14 C. Wang, W. Qi, Y. Zhou, W. Kuang, T. Azhagan, T. Thomas, C. Jiang, S. Liu and M. Yang, *Chem. Eng. J.*, 2020, **381**, 122611.
15 M. Seol, D. H. Youn, J. Y. Kim, J. W. Jang, M. Choi, J. S. Lee and K. Yong, *Adv. Energy Mater.*, 2014, **4**, 1300775.
16 J. Xie, S. Li, X. Zhang, J. Zhang, R. Wang, H. Zhang, B. Pan and Y. Xie, *Chem. Sci.*, 2014, **5**, 4615-4620.
17 Z. Xue, J. Kang, D. Guo, C. Zhu, C. Li, X. Zhang and Y. Chen, *Electrochim. Acta*, 2018, **273**, 229-238.
18 M. Sankar, N. Dimitratos, P. J. Miedziak, P. P. Wells, C. J. Kiely and G. J. Hutchings, *Chem. Soc. Rev.*, 2012, **41**, 8099-8139.
19 J. Jia, M. Zhai, J. Lv, B. Zhao, H. Du and J. Zhu, *ACS Appl. Mater. Interfaces*, 2018, **10**, 30400-30408.
20 J. Zhang, T. Wang, P. Liu, Z. Liao, S. Liu, X. Zhuang, M. Chen, E. Zschech and X. Feng, *Nat. Commun.*, 2017, **8**, 15437.
21 Y. Zhang, B. Ouyang, J. Xu, S. Chen, R. S. Rawat and H. J. Fan, *Adv. Energy Mater.*, 2016, **6**, 1600221.
22 P. Zhou, X. Lv, Y. Gao, Z. Liang, Y. Liu, Z. Wang, P. Wang, Z. Zheng, Y. Dai and B. Huang, *Electrochim. Acta*, 2020, **337**, 135689.
23 M. Hou, R. Lan, Z. Hu and Z. Chen, *Nanoscale*, 2019, **11**, 17093-17103.
24 P. Zhou, X. Lv, D. Xing, F. Ma, Y. Liu, Z. Wang, P. Wang, Z. Zheng, Y. Dai and B. Huang, *Appl. Catal. B*, 2020, **263**, 118330.
25 S. Xue, W. Zhang, Q. Zhang, J. Du, H.-M. Cheng and W. Ren, *Carbon*, 2020, **165**, 112-128.
26 B. Chang, J. Yang, Y. Shao, L. Zhang, W. Fan, B. Huang, Y. Wu and X. Hao, *ChemSusChem*, 2018, **11**, 3198-3207.
27 Y. Gong, L. Wang, H. Xiong, M. Shao, L. Xu, A. Xie, S. Zhuang, Y. Tang, X. Yang, Y. Chen and P. Wan, *J. Mater. Chem. A*, 2019, **7**, 13671-13678.
28 C. Zhu, Z. Yin, W. Lai, Y. Sun, L. Liu, X. Zhang, Y. Chen and S.-L. Chou, *Adv. Energy Mater.*, 2018, **8**, 1802327.
29 Z. Yin, Y. Sun, Y. Jiang, F. Yan, C. Zhu and Y. Chen, *ACS Appl. Mater. Interfaces*, 2019, **11**, 27751-27759.
30 X. Feng, H. Wang, X. Bo and L. Guo, *ACS Appl. Mater. Interfaces*, 2019, **11**, 8018-8024.
31 B. Cao, G. M. Veith, J. C. Neuefeind, R. R. Adzic and P. G. Khalifah, *J. Am. Chem. Soc.*, 2013, **135**, 19186-19192.
32 Y. Wang, Y. Sun, F. Yan, C. Zhu, P. Gao, X. Zhang and Y. Chen, *J. Mater. Chem. A*, 2018, **6**, 8479-8487.
33 C. Giordano, C. Erpen, W. Yao and M. Antonietti, *Nano Lett.*, 2008, **8**, 4659-4663.
34 D. H. Youn, S. Han, J. Y. Kim, J. Y. Kim, H. Park, S. H. Choi and J. S. Lee, *ACS Nano*, 2014, **8**, 5164-5173.
35 P. Giannozzi, S. Baroni, N. Bonini, M. Calandra, R. Car, C. Cavazzoni, D. Ceresoli, G. L. Chiarotti, M. Cococcioni, I. Dabo, A. Dal Corso, S. de Gironcoli, S. Fabris, G. Fratesi, R. Gebauer, U. Gerstmann, C. Gougoussis, A. Kokalj, M. Lazzeri, L. Martin-Samos, N. Marzari, F. Mauri, R. Mazzarello, S. Paolini, A. Pasquarello, L. Paulatto, C. Sbraccia, S. Scandolo, G. Sclauzero, A. P. Seitsonen, A. Smogunov, P. Umari and R. M. Wentzcovitch, *J. Phys. Condens. Matter.*, 2009, **21**, 395502.
36 J. P. Perdew, K. Burke and M. Ernzerhof, *Phys. Rev. Lett.*, 1996, **77**, 3865-3868.
37 N. K. Chaudhari, H. Jin, B. Kim and K. Lee, *Nanoscale*, 2017, **9**, 12231-12247.
38 M. Grden, M. Alsabet and G. Jerkiewicz, *ACS Appl. Mater. Interfaces*, 2012, **4**, 3012-3021.
39 N. Michailidis, F. Stergioudi, H. Omar, D. Missirlis, Z. Vlahostergios, S. Tsipas, C. Albanakis and B. Granier, *Solar Energy Mater. Solar Cells*, 2013, **109**, 185-191.
40 S. A. Shah, X. Shen, A. Yuan, Z. Ji, X. Yue, G. Zhu, H. Zhou, K. Xu, J. Zhu and Y. Chen, *Appl. Surf. Sci.*, 2020, **527**, 146918.
41 Y. Zhao, B. Jin, A. Vasileff, Y. Jiao and S.-Z. Qiao, *J. Mater. Chem. A*, 2019, **7**, 8117-8121.
42 S. Liu, Y. Jiang, M. Yang, M. Zhang, Q. Guo, W. Shen, R. He and M. Li, *Nanoscale*, 2019, **11**, 7959-7966.
43 P. S. Herle, M. Hegde, K. Sooryanarayana, T. Guru Row and G. Subbanna, *Inorg. Chem.*, 1998, **37**, 4128-4130.
44 K. Weil, P. Kumta and J. Grins, *J. Solid State Chem.*, 1999, **146**, 22-35.

45 Z. Yin, Y. Sun, C. Zhu, C. Li, X. Zhang and Y. Chen, *J. Mater. Chem. A*, 2017, **5**, 13648-13658.
46 X. Shi, A. Wu, H. Yan, L. Zhang, C. Tian, L. Wang and H. Fu, *J. Mater. Chem. A*, 2018, **6**, 20100-20109.
47 Y. Huang, J. Ge, J. Hu, J. Zhang, J. Hao and Y. Wei, *Adv. Energy Mater.*, 2018, **8**, 1701601.
48 H. J. Park, S. Y. Lee, T. K. Lee, H.-J. Kim and Y. M. Lee, *J. Memb. Sci.*, 2020, **611**, 118355.
49 G. Bender, M. Carmo, T. Smolinka, A. Gago, N. Danilovic, M. Mueller, F. Ganci, A. Fallisch, P. Lettenmeier, K. A. Friedrich, K. Ayers, B. Pivovar, J. Mergel and D. Stolten, *Int. J. Hydrog. Energy*, 2019, **44**, 9174-9187.
50 S. Siracusano, V. Baglio, A. Di Blasi, N. Briguglio, A. Stassi, R. Ornelas, E. Trifoni, V. Antonucci and A. S. Aricò, *Int. J. Hydrog. Energy*, 2010, **35**, 5558-5568.
51 J. Wang, F. Xu, H. Jin, Y. Chen and Y. Wang, *Adv. Mater.*, 2017, **29**, 1605838.
52 A. Borgschulte, O. Sambalova, R. Delmelle, S. Jenatsch, R. Hany and F. Nuesch, *Sci. Rep.*, 2017, **7**, 40761.
53 J. K. Nørskov, T. Bligaard, A. Logadottir, J. R. Kitchin, J. G. Chen, S. Pandelov and U. Stimming, *J. Electrochem. Soc.*, 2005, **152**, J23-J26.